PHYSICAL REVIEW B **89**, 024104 (2014)

Ab initio modeling of the two-dimensional energy landscape of screw dislocations in bcc transition metals

L. Dezerald,[1] Lisa Ventelon,[1] E. Clouet,[1] C. Denoual,[2] D. Rodney,[3] and F. Willaime[1]
[1]*CEA, DEN, Service de Recherches de Métallurgie Physique, 91191 Gif-sur-Yvette, France*
[2]*CEA, DAM, DIF, Arpajon F-91297, France*
[3]*Institut Lumière Matière, Université Lyon 1, CNRS UMR 5306, 69622 Villeurbanne, France*

(Received 15 November 2013; revised manuscript received 23 December 2013; published 15 January 2014)

A density functional theory (DFT) study of the $1/2\langle 111\rangle$ screw dislocation was performed in the following body-centered cubic transition metals: V, Nb, Ta, Cr, Mo, W, and Fe. The energies of the easy, hard, and split core configurations, as well as the pathways between them, were investigated and used to generate the two-dimensional (2D) Peierls potential, i.e. the energy landscape seen by the dislocation as a function of its position in the (111) plane. In all investigated elements, the nondegenerate easy core is the minimum energy configuration, while the split core configuration, centered in the immediate vicinity of a $\langle 111\rangle$ atomic column, has a high energy near or above that of the hard core. This unexpected result yields 2D Peierls potentials very different from the usually assumed landscapes. The 2D Peierls potential in Fe differs from the other transition metals, with a monkey saddle instead of a local maximum located at the hard core. An estimation of the Peierls stress from the shape of the Peierls barrier is presented in all investigated metals. A strong group dependence of the core energy is also evidenced, related to the position of the Fermi level with respect to the minimum of the pseudogap of the electronic density of states.

DOI: 10.1103/PhysRevB.89.024104 PACS number(s): 61.72.Lk, 31.15.E−

I. INTRODUCTION

Body-centered cubic (bcc) transition metals are known to display an unusual plastic behavior at low temperature, which has long been attributed to the core properties of the $1/2\langle 111\rangle$ screw dislocations [1,2]. One defining feature is that plasticity in bcc metals is strongly thermally activated at low temperatures [3]. The reason is that the motion of screw dislocations is impeded by a high lattice friction, a consequence of the depth of the dislocation Peierls potential, i.e. the energy landscape seen by the dislocation while gliding through the crystal. The Peierls potential, usually written as a one-dimensional (1D) function of the dislocation position, has been modeled using a variety of analytic functions [4,5]. One-dimensional Peierls potentials have also been determined directly in atomistic models based on embedded atom method (EAM) potentials [6–9], bond order potentials (BOP) [10], as well as *ab initio* density function theory (DFT) calculations [11–14].

Another characteristic of plasticity in bcc metals is its anisotropy, best known through deviations to the Schmid law at the origin of a dependence of the critical resolved shear stress on crystalline orientation [2,15]. To capture this effect, the Peierls potential must be generalized to two dimensions (2D), with the dislocation energy expressed as a function of the dislocation position in the full (111) plane perpendicular to the $1/2\langle 111\rangle$ Burgers vector. This approach was pioneered by Edagawa *et al.* [16,17], who showed that combining a line tension model with a 2D Peierls potential based on trigonometric functions that respect the threefold symmetry of the bcc lattice allows one to reproduce both the temperature dependence of the flow stress and the relation between the average slip direction and the maximum resolved shear stress in a number of bcc metals. The same methodology was recently employed by Gröger and Vitek [18] to predict temperature and strain rate effects on the flow stress from BOP calculations.

In the (111) plane, several positions of high symmetry are expected to be extrema of the 2D Peierls potential. These positions are the centers of gravity of the upward and downward triangles of the hexagonal lattice formed by the projections of the [111] atomic columns in the (111) plane. Depending on the sign of the Burgers vector, a screw dislocation located at these positions results in either a local minimum, the easy core, where the chirality of the three [111] atomic columns around the core is reversed compared to the bulk bcc structure, or a local maximum, the hard core, where the three atomic columns around the core are at the same altitude in the [111] direction [1]. Another position of high symmetry is when the dislocation is centered on an atomic column. This position is actually a singular point of the Peierls potential but can be closely approached by the so-called split core [19], which is centered in the immediate vicinity of the atomic column and has three possible orientations [13].

To our knowledge, all published EAM potentials predict the same hierarchy between easy, hard, and split cores: the easy core is the global energy minimum of the 2D Peierls potential, the hard core is the global maximum, and the split core has an intermediate energy. With interatomic potentials that predict a nondegenerate core structure, such as the well-known potentials developed by Mendelev *et al.* [20,21], split cores are local minima, through which the dislocation passes when moving from one easy core position to the next, resulting in 1D Peierls potentials with a camel-hump shape [19,11,6,7]. The only two exceptions that we are aware of are the EAM potentials developed by Chamati *et al.* [22] and Marinica *et al.* [23,24], which are single humped. This hierarchy between easy, split, and hard cores was, however, recently put into question by DFT calculations [12,13], which showed that, in bcc Fe, the hard core energy is low, close, or even below that

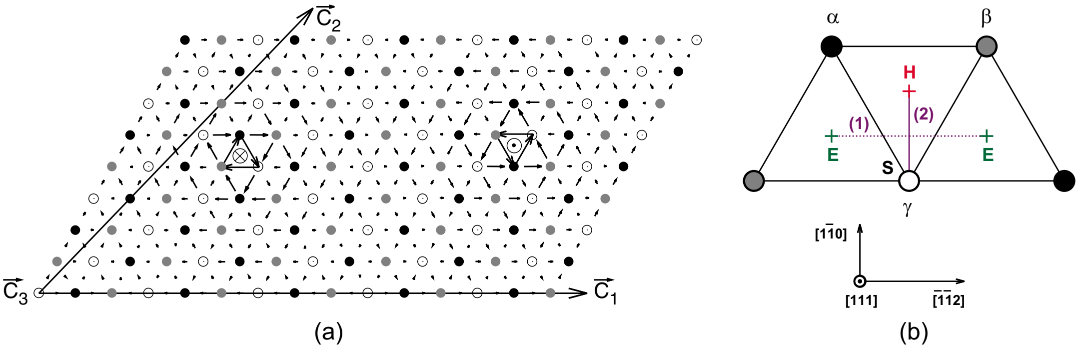

FIG. 1. (Color online) Simulation cell: (a) Schematic representation of the 135-atom simulation cell and periodicity vectors within the quadrupolar arrangement of dislocation dipoles. Atomic positions are represented by three different colors depending on their (111) plane before introduction of the dislocations. The dislocation dipole is visualized by its differential displacement map. (b) Schematic representation of the two investigated pathways: pathway (1) between two neighboring easy core positions (denoted E), and pathway (2) between a hard (denoted H) and a split core configuration (denoted S). The three [111] atomic columns surrounding the hard core are denoted α, β, and γ.

of the saddle configuration between easy cores, while the split core is the global energy maximum. Preliminary calculations in W [13] showed that this inversion of energy between hard and split cores may also be true for other bcc metals. To conclude, a more systematic investigation in all bcc transition metals is required.

In this paper, we perform a systematic study using DFT of the 2D Peierls potential of the $1/2\langle 111\rangle$ screw dislocation in all bcc transition metals: group V vanadium, niobium, and tantalum; group VI chromium, molybdenum, and tungsten; and ferromagnetic iron. In all metals, we computed the energy of the easy, hard, and split cores, as well as the energy pathways between these configurations. Using two different methods to locate the dislocation core along these paths, we generated 2D Peierls potentials based on an interpolation that respects the symmetries of the bcc lattice. The landscapes are compared with the ones usually assumed and are used to extract the Peierls stress.

II. METHODOLOGY

A. DFT technicalities

The present *ab initio* calculations were performed within the DFT framework using the plane wave code PWSCF [25]. The pseudopotentials are ultrasoft with semicore electrons for V, Nb, Ta, Cr, Mo, and W and without semicore electrons for Fe [26]. The calculations in Fe are spin-polarized (ferromagnetic Fe). Cr is treated in the paramagnetic approximation; the results for this metal are therefore given to illustrate the group and series tendencies but should not be considered as accounting for the behavior of real Cr with its complex magnetic structure [27]. For all investigated elements, the exchange-correlation energy was evaluated using the Perdew-Burke-Ernzerhof generalized gradient approximation, with a wavefunction cutoff of 40 Ry. The Hermite-Gauss scheme was employed with a smearing of 0.3 eV to broaden the electronic density of states. Residual forces after relaxation are smaller than 0.01 eV/Å.

The dislocation calculations were performed using a periodic array of dislocation dipoles with a quadrupolar arrangement, which is the most appropriate to extract dislocation properties [28,29]. As illustrated in Fig. 1(a), the simulation supercell contains 135 atoms with triperiodic boundary conditions. The cell vector length along the dislocation line was set to one Burgers vector, $b = \sqrt{3/2}a_0$, where a_0 is the equilibrium lattice parameter (see Table I). The dislocations are separated in the $\langle 211\rangle$ glide direction by a distance of $7.5\sqrt{2/3}a_0$, i.e. ∼17–19 Å depending on the element. The cell vectors $(\vec{C}_1,\vec{C}_2,\vec{C}_3)$ are defined from the unit vectors $\vec{a}_1 = 1/3[\bar{1}\bar{1}2]$, $\vec{a}_2 = 1/2[1\bar{1}0]$, and $\vec{a}_3 = 1/2[111]$. They are chosen to accommodate the plastic strain induced by the dislocation dipole, so as to minimize the elastic energy contained in the

TABLE I. Bulk properties of the investigated elements compared to experimental values (in italics) [38–43]. The lattice parameter a_0 is in ångström, the bulk modulus B and elastic constants C' and C_{44} in GPa, and the cohesive energy E_{coh} in eV/atom. Here, A is the anisotropy ratio, defined as C_{44}/C'. The results in Cr are given both for nonmagnetic (NM) and antiferromagnetic (AFM) calculations.

	a_0	B	C'	C_{44}	A	E_{coh}
V	3.00 *(3.03)*	156 *(157)*	65 *(55.0)*	24 *(43.2)*	0.36 *(0.78)*	5.11 *(5.31)*
Nb	3.31 *(3.29)*	167 *(170)*	56 *(56.8)*	9.5 *(28.4)*	0.17 *(0.5)*	6.81 *(7.57)*
Ta	3.32 *(3.30)*	192 *(191)*	56.5 *(53.0)*	74 *(82.6)*	1.30 *(1.56)*	8.26 *(8.10)*
Cr (NM)	2.85	253	168	96.8	0.58	3.41
Cr (AFM)	2.93 *(2.88)*	146 *(191)*	158.2 *(150.7)*	96.5 *(103.2)*	0.61 *(0.68)*	3.54 *(4.10)*
Mo	3.16 *(3.14)*	261 *(265)*	145 *(145)*	97 *(111)*	0.67 *(0.77)*	6.14 *(6.82)*
W	3.19 *(3.16)*	304 *(308)*	144 *(157)*	137 *(157)*	0.95 *(1)*	8.18 *(8.90)*
Fe	2.85 *(2.87)*	168 *(168)*	48.2 *(49)*	101.9 *(116)*	2.14 *(2.38)*	5.09 *(4.28)*

simulation cell. Their expressions are:

$$\begin{aligned}\vec{C}_1 &= n\vec{a}_1 - q\vec{a}_3,\\ \vec{C}_2 &= \frac{n}{2}\vec{a}_1 + m\vec{a}_2 + \left(\frac{1}{2} - \frac{q}{2}\right)\vec{a}_3,\\ \vec{C}_3 &= \vec{a}_3,\end{aligned} \tag{1}$$

with $(n,m) = (15,9)$ for the 135 atom supercell, and $q = 1/3m$ for the easy core configuration, $q = -1/3m$ for the hard core configuration, and $q = 1/m$ for the split core configuration [13]. The $-q$ and $-q/2$ components along $\vec{a}_3$ of $\vec{C}_1$ and $\vec{C}_2$ come from the $\sqrt{2}/6a_0$ shift along the $[1\bar{1}0]$ direction between the centers of gravity of upward and downward triangles in the (111) plane. The calculations were performed at constant volume, with a $1 \times 2 \times 16$ shifted k-point grid, which yields Peierls barrier energies converged to within 1 meV/b [13].

In agreement with previous DFT calculations [11,14,30–33], the nondegenerate easy core configuration is the stable minimum-energy configuration for the screw dislocation in all investigated elements. With the above crystallography, the easy core, denoted E, is centered on an upward triangle when $\vec{b} = -1/2[111]$, as illustrated in Fig. 1(b). In the following, the easy core is used as reference for both the cell shape [by taking $q = 1/3m$ in Eq. (1)], and the energy (given relatively to the easy core configuration). In Fig. 1(b), the hard core position, denoted H, is centered on a downward triangle. The three surrounding [111] atomic columns are noted α, β, and γ. With this notation, the split core configuration, denoted S, is centered in the immediate vicinity of the atomic column γ.

B. Reaction coordinates

We computed energy profiles between easy core configurations and between hard and split core configurations. These pathways are respectively denoted (1) and (2) in Fig. 1(b). Calculations along pathway (1) were performed by displacing simultaneously the two dislocations so that their elastic interaction energy remains constant at least for a straight trajectory of the dislocation (see the Appendix). The minimum energy path was obtained using the reaction coordinate method [34], whereby the path is discretized in 11 replicas linearly interpolated between the initial configuration $\vec{X}_I$ and the final configuration $\vec{X}_F$, and the energy of each image is minimized in the hyperplane perpendicular to the initial path using the following reaction coordinate:

$$\xi_1 = \frac{(\vec{X} - \vec{X}_{\mathrm{CM}}).(\vec{X}_F - \vec{X}_I)}{||\vec{X}_F - \vec{X}_I||^2}. \tag{2}$$

The position of the center of mass $\vec{X}_{\mathrm{CM}}$ is subtracted to avoid a global translation of the system. The reaction coordinate along this path should not to be mistaken with the dislocation position, see below. This saddle-point search method was shown in Ref. [13] well adapted to identify minimum energy paths for the simple trajectories considered here. In the case of Cr, this procedure failed because the two dislocations did not move simultaneously (for a reason which is not clear at this point). We therefore used a final configuration, where only one dislocation has moved, and corrected the energies to account for the variation of the elastic energy.

The hard core energy was evaluated by forcing the positions along $\vec{b}$ of the atoms in the three [111] columns surrounding the dislocation core [columns α, β, and γ in Fig. 1(b)] to be fixed, while relaxing all other degrees of freedom. The split core configuration was generated from the hard core configuration by adding relative displacements along $\vec{b}$ of $b/6$ to column α and $-b/6$ to column β and relaxing again all degrees of freedom other than the height of the α, β, and γ atomic columns. The split core energy has been shown to be a good approximation of the dislocation energy close to the atomic column position γ [19,13]. In order to investigate the pathway going from the hard to the split core configurations [denoted pathway (2) in Fig. 1(b)], the path was discretized in six configurations interpolating between the hard and split cores. We should note that, in this case, the two dislocations of the dipole move in opposite $[1\bar{1}0]$ directions, such that their separation distance varies along the path, implying not only a variation of their elastic interaction, but also a variation of the stress in the simulation cell because of the fixed periodicity vectors. The energy relaxations were performed fixing the position of columns α, β, and γ along $\vec{b}$ and relaxing all other degrees of freedom. Along this path, the reaction coordinate is defined as:

$$\xi_2 = \frac{z(\alpha) - z(\beta)}{\frac{b}{3}}, \tag{3}$$

where $z(\alpha)$ [respectively, $z(\beta)$] is the coordinate of column α [respectively, β] along the [111] direction. This reaction coordinate varies between 0 and 1 between the hard and split core configurations since, for the hard core, the three columns α, β, and γ are at the same altitude, so that $\xi_2 = 0$, while for the split core, the relative displacement between columns α and β is $b/3$, so that $\xi_2 = 1$.

As will be seen below, within DFT, energy profiles along pathway (1) have a single maximum (saddle) located halfway between the initial and final easy core configurations. At this location, pathway (1) crosses pathway (2), allowing the reaction coordinate in Eq. (3) to be computed for the saddle configuration. In the following, we call this quantity ξ_2^{saddle}, the split coefficient of the saddle configuration, which we use as a measure of the distance of the saddle configuration to the split core.

C. Elastic correction

The energy profiles along pathways (1) and (2) were computed with a fixed cell shape between initial and final configurations, adjusted in all cases on the easy core configuration, i.e. with $q = 1/3m$ in Eq. (1). Because the cell shape should depend on the dislocation positions in the cell, the displacement of the dislocations in a fixed cell induces an additional energy of elastic nature. A second elastic energy term is induced when the dipole extension (i.e. the distance between dislocations) varies along the path and modifies the elastic interaction. Both terms should be corrected in order to obtain accurate energy paths.

The above elastic energy terms were computed within anisotropic elasticity. Details are given in the Appendix and

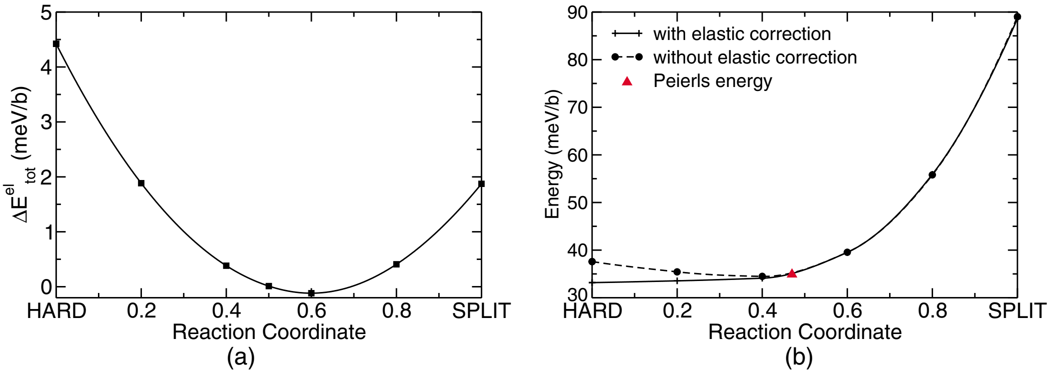

FIG. 2. (Color online) Energy profile along pathway (2) in Fe: (a) elastic energy correction (see the Appendix for details) and (b) energy variation with (solid line) and without (dashed line) the elastic correction.

Refs. [29] and [35]. In brief, along pathway (2) we corrected the DFT energy difference between the current and easy core configurations $\Delta E_{\mathrm{DFT}}(\xi_2)$ by the anisotropic elastic energy difference between these configurations $\Delta E^{\mathrm{el}}_{\mathrm{tot}}(\xi_2)$, that is:

$$\Delta E_{\mathrm{corr}}(\xi_2) = \Delta E_{\mathrm{DFT}}(\xi_2) - \Delta E^{\mathrm{el}}_{\mathrm{tot}}(\xi_2). \tag{4}$$

As an example, the elastic correction $\Delta E^{\mathrm{el}}_{\mathrm{tot}}(\xi_2)$ along pathway (2) in Fe is shown in Fig. 2(a), where it is seen that the correction increases near both the hard and split cores. As shown in the Appendix, the correction decreases in larger simulation cells but can be as large as 5 meV/b in the 135 atom cell used here. In the Appendix, we also compare the present hard core configuration energies computed in the easy cell [i.e. with $q = 1/3m$ in Eq. (1)] with and without elastic correction to that computed in the hard cell [i.e. with $q = -1/3m$ in Eq. (1)], showing that the elastic correction accounts for most of the cell shape effect. A similar correction arises along pathway (1) from the fact that the dislocation position deviates from a straight trajectory, but the correction is lower than 1 meV/b and will be neglected here.

As shown in Fig. 2(b), the elastic correction induces a significant decrease of the energy near the hard core, so that after correction, the hard core in Fe has an energy slightly lower than the saddle found along pathway (1). The energy difference is, however, close to the precision of the present calculations, which confirms the marked flatness of the energy profile between hard and saddle configurations in Fe discussed in Ref. [13]. As a consequence, the hard core appears to be a monkey saddle for the screw dislocation in Fe. We will see below, however, that this feature is specific to Fe.

D. 2D energy landscape

In order to deduce the Peierls stress and the 2D energy landscape of the dislocation from the DFT energy profiles, the dislocation position in the (111) plane was determined using the two methods presented in Ref. [13]: the cost function and disregistry methods. The cost function method consists in comparing the relative displacements of the five most displaced $\langle 111\rangle$ atomic columns [8] to that predicted by anisotropic elasticity. The resulting cost function is minimized with respect to the dislocation core position in the (111) plane. The second method consists in comparing the disregistry that corresponds to the difference of displacement between the two $\{110\}$ atomic planes directly above and below the glide plane of the dislocation, to solutions of an elastic model similar to the Peierls-Nabarro model.

Applying these methods along the 1D profile of pathway (1), we obtain the Peierls potential, i.e. the dislocation energy as a function of its position in the glide direction x, from which we can estimate the Peierls stress:

$$\sigma_P = \max\left(\frac{1}{b}\frac{\partial E(x)}{\partial x}\right). \tag{5}$$

Here, we neglect any dependence of the Peierls potential on the applied stress [6,11]. Along pathway (2), the dislocation position obtained with both the disregistry and cost function methods coincides with that given by the reaction coordinate ξ_2.

The 2D energy landscape is obtained by interpolation of the dislocation energy along pathways (1) and (2) using the following numerical fit, which takes into account the periodicity and threefold symmetry of the bcc lattice.

Smooth surfaces are efficiently represented by a Fourier decomposition:

$$E(\vec{r}) = \sum_{n,m} F(\vec{k}_{n,m})\exp(2\pi i\vec{k}_{n,m}.\vec{r}), \tag{6}$$

where $\vec{k}_{n,m} = n\vec{b}_1 + m\vec{b}_2$ are wave vectors in reciprocal space, and the reciprocal vectors $\vec{b}_i$ are defined from the periodicity vector $\vec{a}_i$ of the Peierls potential through the canonical relation $\vec{a}_i.\vec{b}_j = \delta_{ij}$. If one considers a limited set of wave vectors, the amplitudes $F(\vec{k}_{n,m})$ can be easily determined by a least square minimization. It is, however, delicate to choose the number and location of the wave vectors, a too-rich representation leading to spurious modes, whereas missing frequencies dramatically increase the error between data and interpolation. To avoid this problem, we minimize the sum of the least square error and the square of the Laplacian (computed in the reciprocal space) over a large domain of frequencies:

$$\varepsilon(\lambda) = \sum_G [E(\vec{r}_G) - E_G]^2 + \lambda\int_S dS[\Delta E(\vec{r})]^2, \tag{7}$$

where $\vec{r}_G$ is the coordinate of the G^{th} interpolation point (of energy E_G), and λ is a weight factor. Increasing λ favors a smooth interpolation at the expense of the quality of the interpolation. In this study, the weight λ was automatically adjusted so that the maximum distance $\max_G \|E(\vec{r}_G) - E_G\|$ was less than a prescribed value, e.g. 1% of the maximum amplitude of E. The resulting interpolation is thus the smoothest with a prescribed maximum error.

III. RESULTS

A. Bulk properties

As a preliminary work, the bulk properties of all investigated elements were calculated using DFT. The bcc elastic constants C' and C_{44} were calculated by applying, respectively, tetragonal and trigonal distortions of ±2%. The results are displayed and compared to experimental data in Table I. The DFT results are in good agreement with the experimental data in all investigated elements, except for group V vanadium and niobium, for which the elastic constants C' and C_{44} are underestimated, as reported by other authors in the literature [32,14,36,37]. Results for vanadium and niobium are therefore presented as the first available calculations, without claiming to be fully predictive.

B. Dislocation core properties

To study the properties of the easy core configuration, we computed its core energy and formation volume in all investigated metals. Core energies were extracted using the methodology proposed in Ref. [29]. Formation volumes per unit length of dislocation, both perpendicular ($V_\perp$) and parallel ($V_\parallel$) to the dislocation line, were defined from the strains deduced from the stresses computed in the DFT simulations with the help of the elastic compliances [29]:

$$V_\perp = \frac{\varepsilon_{11} + \varepsilon_{22}}{2} S, \quad V_\parallel = \frac{\varepsilon_{33}}{2} S, \tag{8}$$

where S is the cell surface perpendicular to the [111] direction.

The results are given in Table II. We can see that inserting a screw dislocation is systematically associated with a positive formation volume $V_\perp$, i.e. a dilatation in the (111) plane perpendicular to the dislocation line. The dilatation is large, close to 0.5 b^2, in Mo, W, and Fe. This effect has already been reported for Fe within DFT in Refs. [29,44] but is in general not observed with empirical potentials. The fact that this large dilatation is not specific to Fe shows that this effect is not due to magnetism. Nb displays the largest dilatation volume in the (111) plane, while Ta has the smallest dilatation volume. These differences can be better understood by visualizing the displacements of the atoms in the (111) plane, as illustrated for Ta and W in Fig. 3. In Ta, the displacements are limited to the first two shells of atoms near the dislocation core while in W, the displacements are much longer ranged, resulting in a larger formation volume.

TABLE II. Easy core properties: formation volumes per unit length of dislocation, perpendicular $V_\perp$ and parallel $V_\parallel$ to the dislocation line expressed in units of b^2. Easy core energies E_{core} are also given in meV/b.

	$V_\perp$	$V_\parallel$	$\frac{V_\perp}{V_\parallel}$	$-\frac{C'_{33}}{C'_{13}}$	E_{core}
V	0.34	−0.27	−1.29	−1.30	103
Nb	1.21	−0.81	−1.48	−1.13	201
Ta	0.19	−0.05	−4.12	−2.07	143
Mo	0.45	−0.27	−1.66	−2.08	423
W	0.40	−0.22	−1.81	−2.37	523
Fe	0.47	−0.11	−4.14	−3.16	192

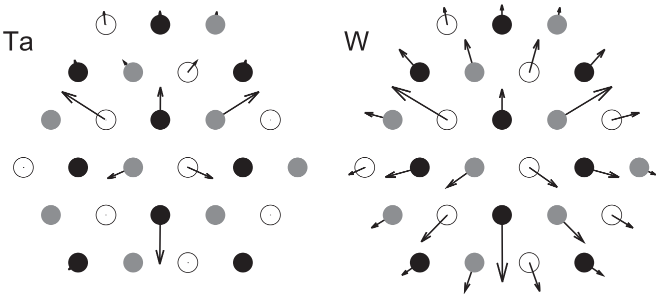

FIG. 3. Edge displacement maps of the easy core configuration as obtained from DFT calculations after subtraction of the Volterra elastic field, for Ta and W. Vectors correspond to the (111) in-plane displacement, magnified by a factor 50. Displacements smaller than 0.01 Å are omitted for clarity.

Dilatations in the (111) plane are associated with contractions in the direction parallel to the dislocation line, i.e. negative $V_\parallel$, as expected from Poisson's effect. The ratio between $V_\perp$ and $V_\parallel$, however, does not necessarily follow quantitatively linear elasticity, which predicts [29]:

$$\frac{V_\perp}{V_\parallel} = -\frac{C'_{33}}{C'_{13}}, \tag{9}$$

where C'_{ij} are the elastic constants in the dislocation coordinate system. This prediction is compared with the DFT calculations in Table II, where we can see that, while the ratios are quite close in V and Nb, they can be up to a factor 2 different in other elements, in particular Ta.

Easy core energies, calculated for a cutoff radius equal to b, are reported in Table II and shown in Fig. 4(a) after normalization by E_{coh}/b, where E_{coh} is the cohesive energy, in order to evidence the effect of electronic band filling. Strikingly, group VI elements (Mo, W) have normalized core energies approximately three times larger than group V elements (V, Nb, Ta). This can be explained by investigating the local density of states (LDOS) of the atoms surrounding the dislocation core, as illustrated in Nb and Mo in Fig. 5. The bulk DOS is similar in all bcc transition metals with a marked pseudogap responsible for the stability of the bcc structure close to half-band filling. In the LDOS of the atoms in the dislocation core, the pseudogap is partially filled as shown in Fig. 5. In group VI Mo (and likewise W), the Fermi level E_F is close to the minimum of the pseudogap, leading to a large increase of the band-energy contribution to the total energy compared to the bulk (since bonding states far from E_F are replaced by states closer to E_F, i.e. with a larger band energy). The effect is weaker, or even possibly reversed, in group V elements as Nb where the Fermi level is shifted from the LDOS minimum. This situation is the same as for the vacancy

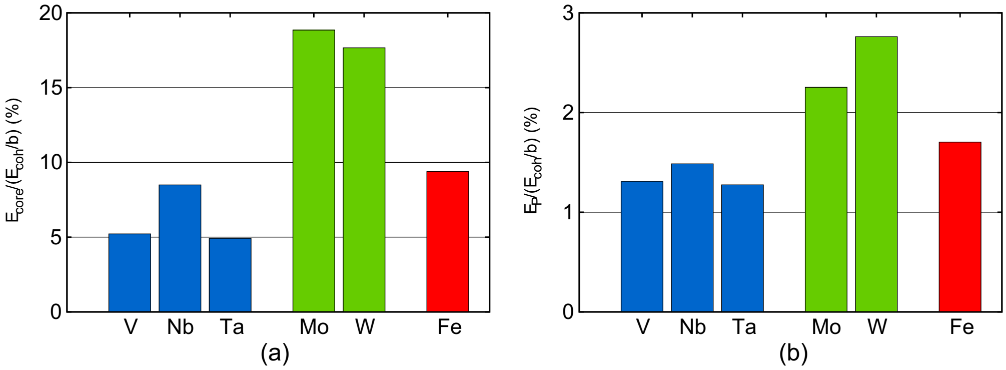

FIG. 4. (Color online) Group dependence of the normalized energy for (a) easy core energy and (b) Peierls energy.

formation energy, with values normalized to E_{coh} larger in group VI than in group V [45].

C. 1D energy profiles

1. Peierls barriers—pathway (1)

The energy profiles along pathway (1) between two successive easy core configurations are shown in Fig. 6. Both relaxed and unrelaxed profiles are shown because they exhibit a pronounced group dependence, with relaxations more important for group V elements than for group VI. This group dependence of the relaxation around a defect is again similar to what occurs for vacancies [45–47]. The weak relaxation in group VI is attributed to angular forces, which are not accounted for in EAM potentials for instance.

All energy profiles have a single maximum, in agreement with Refs. [11–14], located halfway between the initial and final easy core configurations. The saddle configuration between easy cores is thus systematically at the intersection with pathway (2) between the hard and split cores. In contrast with Ref. [14], however, while some profiles are close to sinusoidal (Fe, Ta, and W), others are clearly not sinusoidal (V, Cr, Nb, and Mo). The nonsymmetric profile obtained for Cr arises from the different methodology used for this element where it was not possible to have both dislocations moving simultaneously (Sec. IIB): the obtained profile should be considered as approximate—for this reason and also because we use the paramagnetic approximation.

The energies of the saddle configurations, i.e. the Peierls energies, are given in Table III and shown in Fig. 4(b) normalized by E_{coh}/b. We see again a dependence on band filling: the normalized Peierls energy in group VI elements is more than twice that of group V elements. It should be noted that the normalized core energy is about five times larger than the normalized Peierls energy. We checked that this is because the density of states varies much less when the dislocation moves from one easy core to another one than when a dislocation is introduced in the perfect crystal.

To further characterize the saddle configurations, we report in Table III their split coefficients, computed from Eq. (3). We see again a group tendency: V and Nb (group V) have a large split coefficient ($\xi_2^{\mathrm{saddle}} > 0.6$), while Cr, Mo, and W (group VI) have an intermediate split coefficient ($0.5 < \xi_2^{\mathrm{saddle}} < 0.6$). Fe and Ta have atypical behaviors since Ta, although from group V, has a small split coefficient, and Fe has a very small split coefficient, below 0.5. We also note that elements with a large split coefficient (V and Nb) tend to have a flat Peierls potential near the saddle. In the extreme case when the split configuration is a local minimum, as with the Mendelev EAM potentials [20,21], the configuration halfway across the path becomes the split core (i.e. $\xi_2^{\mathrm{saddle}} = 1$) and the curvature of the Peierls potential, which adopts a camel-hump shape,

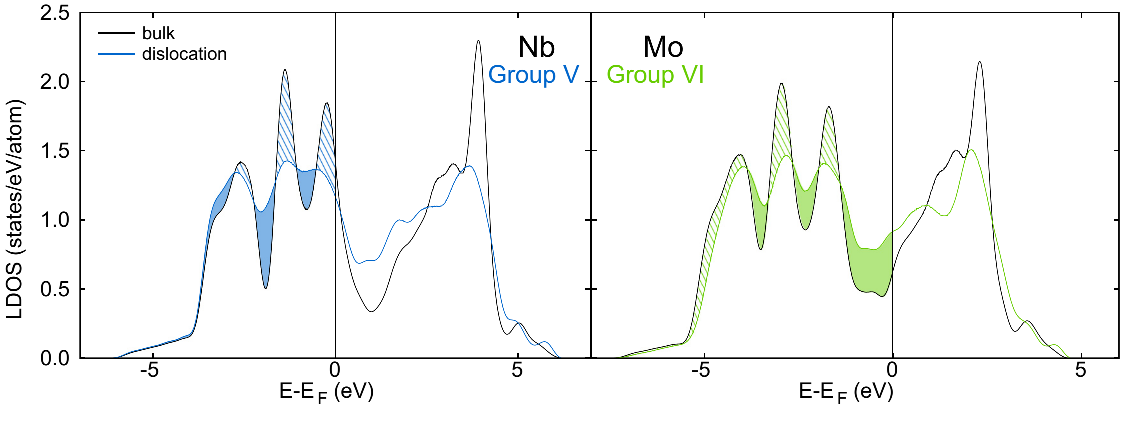

FIG. 5. (Color online) Local density of states for atoms α, β, and γ of Fig. 1(b) around the dislocation core compared to the bulk (black; all three atoms share the same LDOS) in Nb and Mo. Energies are given with respect to the Fermi energy (color).

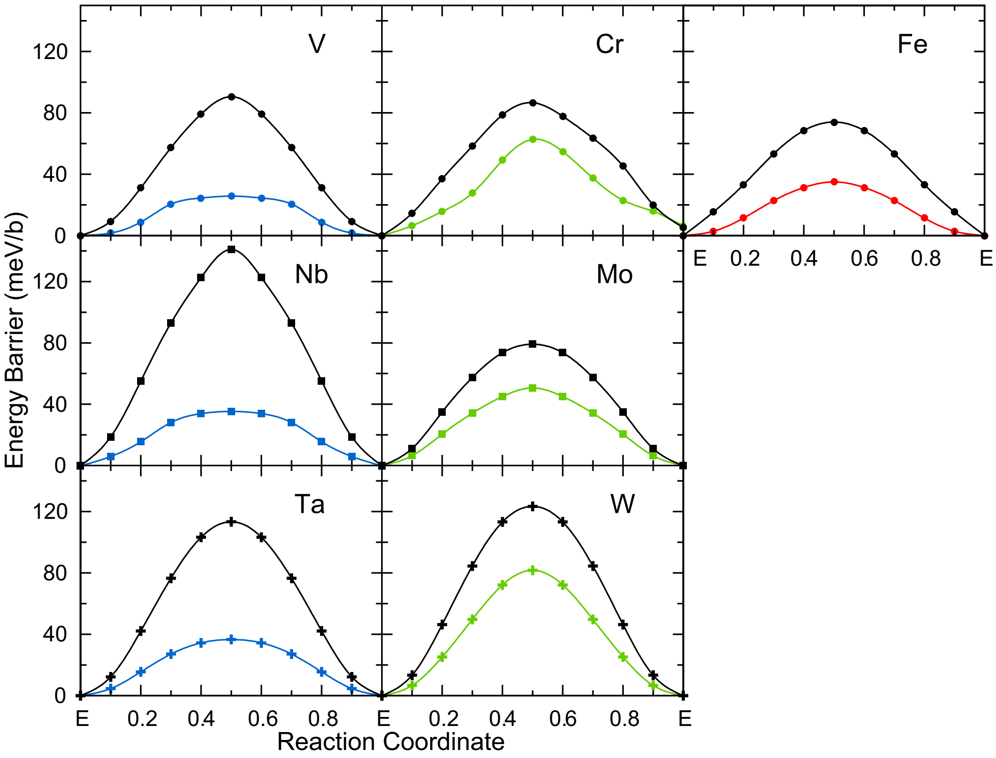

FIG. 6. (Color online) Peierls barrier of the $1/2\langle 111\rangle$ screw dislocation in bcc transition metals before (black) and after relaxation (color).

changes sign. There is thus a strong correlation between the curvature of the Peierls potential at the saddle configuration and its proximity to the split core, which in turn is related to the deviation of the dislocation path in the (111) plane from a straight trajectory between easy cores to a bent path that passes through the split core.

2. Hard to split core energy profiles—pathway (2)

The hard and split core energies are listed in Table III, and the energy profiles between these two cores along pathway (2) are shown in Fig. 7 as a function of the reaction coordinate in Eq. (3). These energies include elastic corrections as explained in Sec. IIC. In Fig. 7, all energies are normalized by the hard core energy to allow for easier comparison between elements.

For all investigated metals, the split core is an energy maximum with a nonzero first derivative because of the singularity associated with this point. With the limitation that the shear modulus in V and Nb is underestimated compared to the experiments, our calculations show that group V elements, V and Nb, have a split core energy close to that of the hard

TABLE III. Energy of the following configurations: split core E_S, hard core E_H, and saddle point E_P—i.e. the Peierls energy—relative to the easy core in all bcc transition metals, expressed in meV/b. The elastic correction (described in Sec. IIC and the Appendix) is included in the hard core and split core energies. The last column displays the split coefficient of the saddle configuration ξ_2^{saddle} [see Eq. (3)].

	E_S	E_H	E_P	ξ_2^{saddle}
V	51.3	52.5	25.7	0.63
Nb	81.8	76.3	35.2	0.68
Ta	67.0	44.0	36.6	0.51
Cr	154.6	102.2	62.7	0.58
Mo	147.6	88.2	50.5	0.57
W	208.5	128.6	81.8	0.55
Fe	87.9	33.2	34.9	0.47

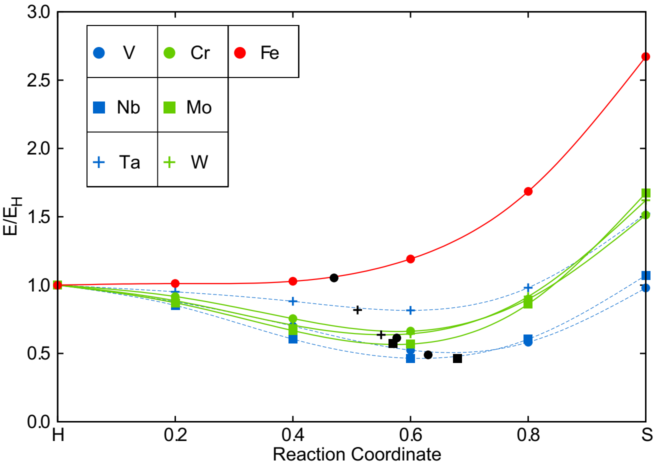

FIG. 7. (Color online) Energy variation between the hard and split cores [pathway (2)]. The energies are normalized by the hard core energy. The black symbols correspond to the saddle configurations obtained along pathway (1). The blue dashed lines correspond to group V elements, the green solid lines correspond to group VI elements, and the red solid line corresponds to Fe.

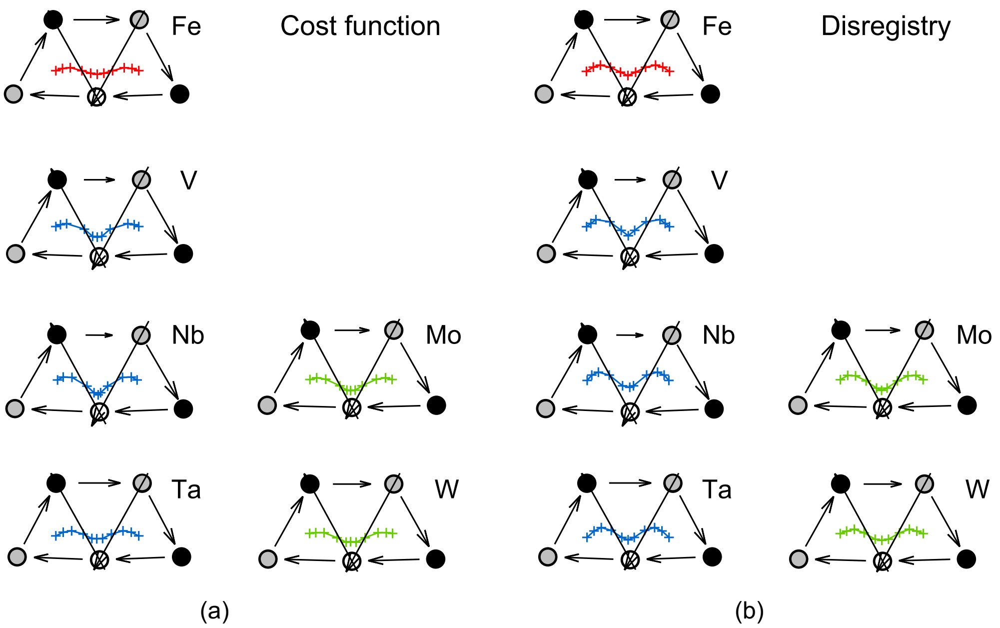

FIG. 8. (Color online) Dislocation trajectory using (a) the cost function method and (b) the disregistry method. The differential displacement maps correspond to the saddle configuration for each element.

core. For group VI elements, together with Ta and Fe, the split core has an energy more than 1.5 times higher than the hard core. This result, already reported for Fe and W in Ref. [13], is highly unexpected because it contradicts all interatomic potentials published so far, which systematically predict that the hard core is the configuration of maximum energy. Moreover, most interatomic potentials that predict a stable nondegenerate easy core structure also predict that the split core is a local minimum [19,48]. In contrast, we see here that DFT calculations systematically predict that the split core is a maximum, with an energy close or higher than the hard core.

For group V and VI elements, the energy variation between the hard and split core configurations evidences a minimum between $\xi_2 = 0.5$ and 0.7, which should correspond to the saddle configuration of pathway (1) if the calculations along pathways (1) and (2) are consistent. We checked this point by adding to Fig. 7 the energies of the saddle configurations found on pathway (1) as a function of their split coefficient. Except for Fe, the position of the saddle along pathway (1) is indeed close to the minimum of the energy profile along pathway (2). The discrepancy in Fe can be explained by the fact that the saddle point along pathway (1) corresponds to the minimum along pathway (2) before applying the elastic correction. In Fe, this elastic correction shifts the minimum energy along pathway (2) from a split coefficient $\xi_2 \sim 0.5$ to the hard core where $\xi_2 = 0$ (Fig. 2). The effect associated with this elastic correction is less pronounced in other transition metals as the energy profile close to the saddle point is not as flat as in Fe, and the saddle point is located at a place where the elastic correction is less important than in Fe. In order to obtain a more accurate path, it would be necessary to include the elastic correction to the DFT energy during the minimization process. However, this option is technically difficult because of the uncertainty associated with the definition of the dislocation position.

Also, it has to be noted that the split coefficient at the saddle is related to the energy difference between hard and split cores. As the ratio between the split and hard energies decreases, the split coefficient at the saddle increases, which means that the saddle configuration is closer to the split configuration in metals where the energy difference between hard and split cores is smaller.

D. Dislocation trajectory in the (111) plane

As introduced in Sec. IID, the position of the dislocation was evaluated using two methods, the cost function and disregistry methods. The resulting dislocation trajectories in the (111) plane along pathway (1) are displayed in Fig. 8. The trajectories predicted by both methods are quite similar. The trajectories pass close to the γ atomic column, i.e. the split configuration, when the split coefficient at the saddle is high, as e.g. in V and Nb, compared to Mo and W. On the other hand, the dislocation trajectory is closer to linear in Fe and Ta, for which the split coefficient at the saddle is near 0.5. Along pathway (2), we recall that the trajectory is straight between hard and split cores by construction and the position of the dislocation obtained from the cost function method is exactly that given by the reaction coordinate ξ_2.

The energy as a function of the dislocation position is plotted in Fig. 9 for both the cost function and disregistry methods. The departure of these profiles from sinusoidal curves is more marked than when the energy is plotted as a function of the reaction coordinate (Fig. 6). For V, Ta, and Fe, the disregistry and cost function methods give similar results, while in Nb, Mo, and W, a discrepancy is evidenced, in particular close to the reduced core position 0.3. Further tests with the cost function method were performed adjusting the elastic solution on either three or four $\langle 111 \rangle$ atomic columns instead of five as in Ref. [13], but the results are identical.

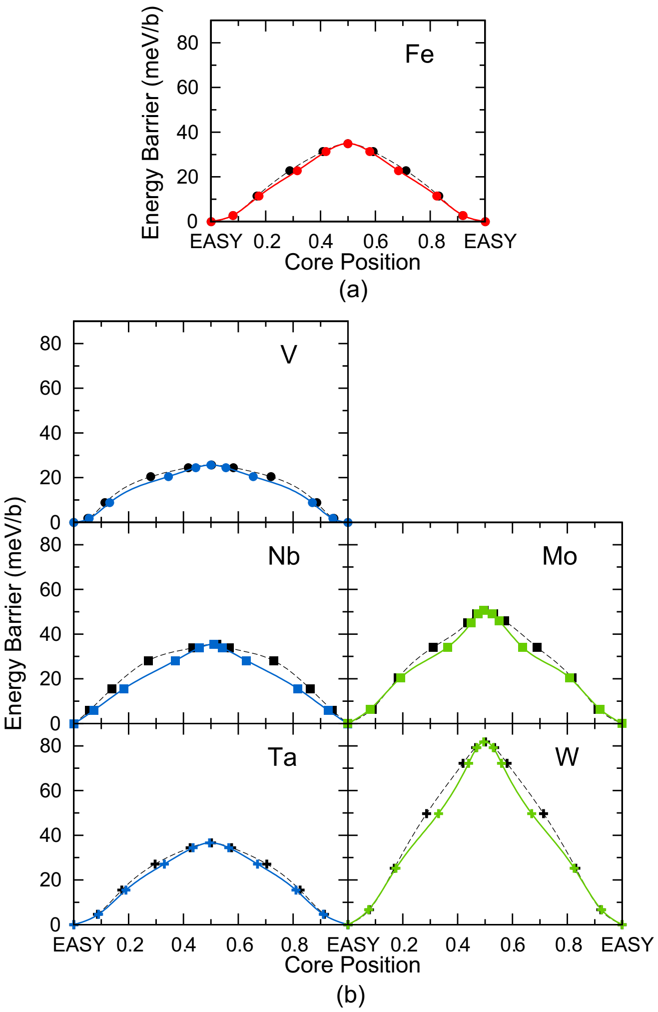

FIG. 9. (Color online) Energy variation between two neighboring easy core positions as a function of the dislocation position (a) for Fe and (b) for nonmagnetic bcc transition metals. The paths are expressed as a function of the dislocation position along the $[\bar{1}\bar{1}2]$ direction determined using the cost function (solid colored lines) and the disregistry (dashed black lines) methods.

Peierls stresses for all investigated metals were evaluated using the maximum derivative of the energy as a function of the dislocation position [Eq. (5)]. They are listed in Table IV. From the difference obtained between the two methods to locate the dislocation, we estimate that the Peierls stress is evaluated with an error on the order of 20%. Peierls stresses were not computed in Mo and only with the disregistry method in W because of the nonsmooth shape of the corresponding 1D Peierls potentials (see Fig. 9). The results evidence the well-known discrepancy between calculated and experimental Peierls stresses, with the former being two to three times larger than the latter. Proville *et al.* [23] recently showed that the discrepancy arises from quantum corrections, but the simulation cell required to evaluate such correction (approximately 10^5 atoms) is too large to be considered with DFT for now.

TABLE IV. Peierls stresses in MPa deduced from the maximum slopes of the 1D Peierls potentials plotted using either the cost function method or the disregistry method. The experimental data come from Refs. [49–54].

	Cost function	Disregistry	Experimental
V	1000	1200	360
Nb	650	860	450
Ta	810	920	350
Mo	/	/	870
W	/	1800	900
Fe	1090	1220	420

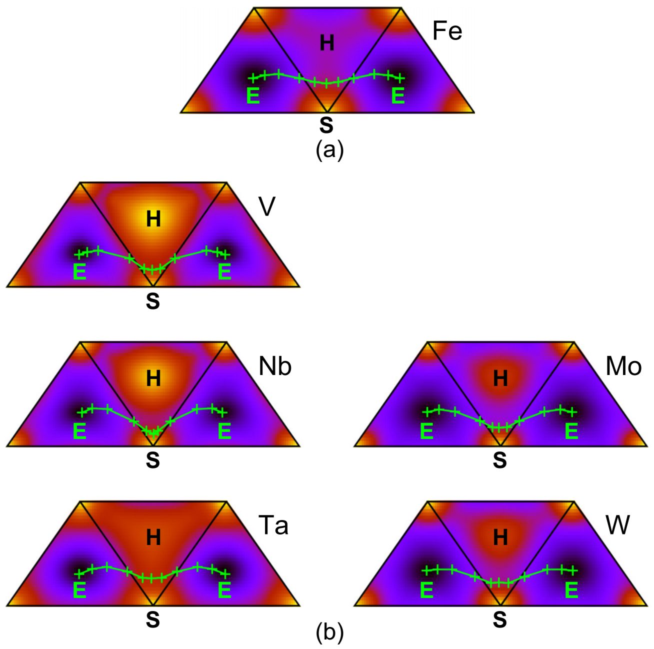

FIG. 10. (Color online) Projections of the 2D Peierls potentials in the (111) plane for (a) Fe and (b) nonmagnetic transition metals. Colors scale with energy going from the minimum (dark) to the maximum energy (light), which depends on the element considered. The dislocation trajectory from the cost function method along pathway (1) is shown in green (same as in Fig. 9).

E. 2D Peierls potential

The 2D Peierls potentials were obtained using the numerical interpolation presented in Sec. IID from the energy profiles along pathways (1) and (2) as a function of the dislocation position obtained with the cost function method. It should be recalled that the positions in the (111) plane corresponding to atomic columns are singular points. We identify here these positions with the split core, which is itself ill-defined since this core can take three different configurations depending on the easy core it is connected to. All three variants are located in the immediate vicinity of the atomic column and have the same energy. We thus associate this energy to the atomic column position. Also, even though the method to locate the dislocation influences the energy profiles as seen in Fig. 9, these profiles can be used to display the general tendency and shape of the 2D Peierls potentials. The resulting potentials are shown in projection in Fig. 10 and in perspective in Fig. 11.

The 2D Peierls potentials display the same tendencies as observed on the 1D plots: for all investigated elements, the split

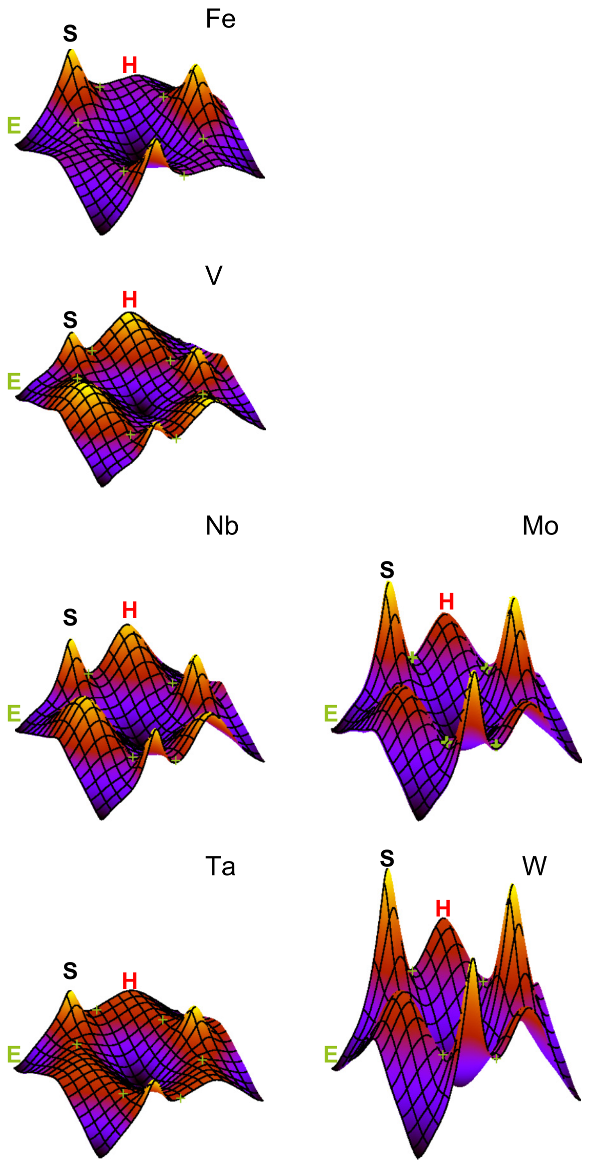

FIG. 11. (Color online) 2D Peierls potentials for Fe and nonmagnetic bcc transition metals. All curves are represented using the same energy scale. The color scale is the same as in Fig. 10.

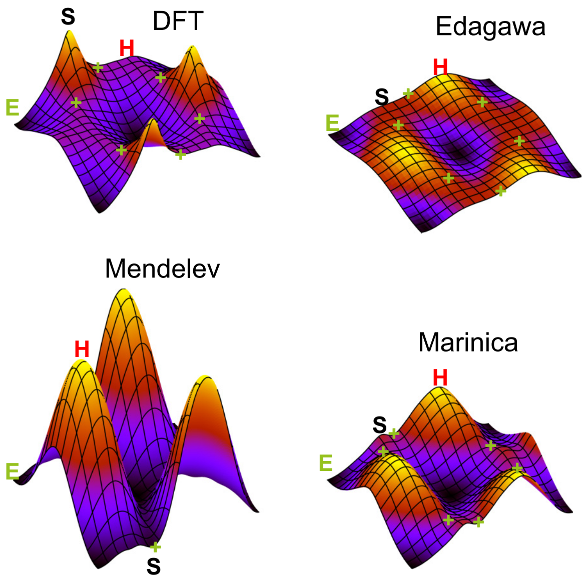

FIG. 12. (Color online) Peierls potentials in Fe adjusted from the present DFT calculations, from the analytical fit of Ref. [16], and from Mendelev [20] and Marinica potentials [23].

core is the maximum energy configuration, and in group V and VI elements, the hard core configuration is a local maximum. Fe has an atypical behavior with a very flat potential around the hard core position. In Fig. 12, the 2D Peierls potential for Fe obtained with DFT is compared to the simple analytical potential proposed by Edagawa *et al.* [16] and often used in the literature (see, for instance, Ref. [18]). This potential, written as a product of sinusoidal functions, is a Fourier expansion as in Eq. (6) limited to a single harmonic ($-1 \leqslant n,m \leqslant 1$) with purely imaginary coefficients. We also added the potentials obtained with the present fitting methodology when representing atomic bonding by two different EAM potentials, Mendelev [20] and Marinica [23] potentials. The 2D Peierls potential proposed by Edagawa and those fitted on EAM data are qualitatively similar, with a global maximum at the hard core position, although the height of this maximum depends on the potential: not strongly marked on Edagawa's potential, very high with Mendelev potential, and intermediate with Marinica potential. The split core on the other hand is of different nature: a monkey saddle on Edagawa's potential, a local minimum with Mendelev potential, and a local maximum with Marinica potential, however weakly marked. These features are very different from the present DFT calculations, which show that the split core is the true maximum and that the hard core is a monkey saddle. Such a 2D potential is incompatible with the simple expression proposed by Edagawa in Ref. [16]. However, Edagawa generalized the expression of the 2D Peierls potential by introducing a nonzero phase in the sinusoidal functions of the first harmonic [17]. This is equivalent to consider Fourier coefficients with both real and imaginary parts. This allows us to reproduce, at least qualitatively, the DFT potential for Fe and the other transition metals considered here. A more in-depth analysis of the properties of these potentials will be the subject of a future publication.

IV. SUMMARY AND CONCLUSIONS

In this paper, the core structure and 2D energy landscape of $1/2\langle 111\rangle$ screw dislocations were investigated in all bcc transition metals V, Nb, Ta, Cr, Mo, W, and Fe using DFT calculations. The stable configuration was found to be the nondegenerate easy core configuration, in good agreement with previous DFT calculations.

The normalized dislocation core energy displays unexpected group tendencies, as it depends on the position of the Fermi level with respect to the minimum of the pseudogap of the electronic density of states. Group VI elements, for which the Fermi level is close to the minimum of the pseudogap, display core energies around three times higher than group V elements. The 2D Peierls potential was investigated using two 1D cross-sections: the Peierls barriers and the pathway joining the hard to the split core configurations. The Peierls barriers were shown to be single-humped in all investigated elements. Their relaxations exhibit pronounced group dependence, with weaker relaxation in group VI than in group V. Again, a dependence on band filling was evidenced on the normalized Peierls energy amplitudes.

The splittings of the dislocation core were evaluated halfway through the Peierls barriers, and the dislocation trajectories in the (111) plane were evaluated using the disregistry and the cost function methods. These calculations evidenced a strong correlation between the curvature of the Peierls barrier near the saddle configuration, the proximity of the saddle to the split core, the ratio between the split and hard core energies, and deviations from a straight path between easy core configurations. The usual ordering between hard core and split core energies is thus revisited and is shown to influence the shape of the transition path. In a nutshell, in elements where the split core has an energy close to the hard core (V and Nb), the curvature of the 1D Peierls potential is low, the saddle is close to the split core, and the path is curved, while it is the opposite in Fe or Ta, where the split core has a high energy.

The resulting 2D Peierls potentials are notably different from the usual picture, which is, however, mostly based on empirical potentials. The main and most striking difference is that, in all investigated elements, the split core is the marked maximum with an energy close or above that of the hard core.

Finally, we note that Fe has an atypical behavior for three reasons: (1) it is the only element which does not show a minimum between the hard and split cores, (2) the energy profile is very flat between the hard core and the saddle configuration around the hard core, in the split core direction, and (3) the split core in Fe has a particularly high energy, more than twice that of the hard core.

ACKNOWLEDGMENTS

This work was funded by the European Fusion Materials Modeling programme. The authors would like to acknowledge support from the Partnership for Advanced Computing in Europe (PRACE) for awarding us access to resource MareNostrum III based in Spain at the Barcelona Supercomputing Center (BSC) within the DIMAIM project. L.D. acknowledges M.-C. Marinica (CEA, Saclay, France) for technical assistance and fruitful discussions.

APPENDIX

1. Elastic correction on pathways (1) and (2)

An elastic correction needs to be applied on the energy barriers on pathways (1) and (2) so as to withdraw the variation of the elastic energy on these pathways. The elastic energy does not remain constant because the distance between the two dislocations composing the dipoles varies. On pathway (1), between two easy core configurations, dislocations follow a trajectory not too far from a horizontal straight line (Sec. III D). As a consequence, the distance between them does not vary too much, leading to a variation of the elastic energy less than 1 meV/b. As this corresponds to the estimated accuracy of the DFT calculations, the elastic correction is neglected along pathway (1). On the other hand, variations along pathway (2) are more important and need to be accounted for (Fig. 2).

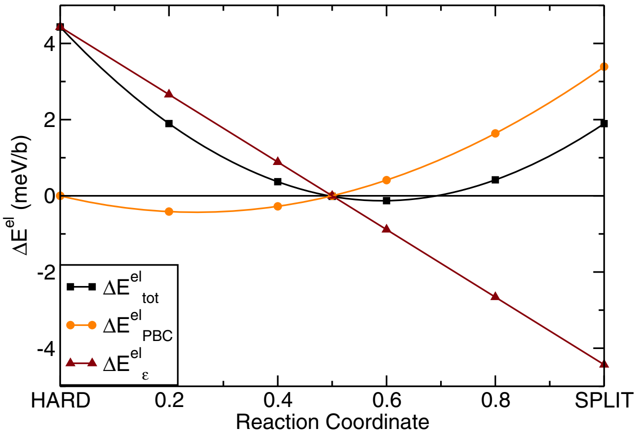

FIG. 13. (Color online) Total elastic correction $\Delta E^{\mathrm{el}}_{\mathrm{tot}}(\xi_2)$ and its decomposition calculated in Fe using anisotropic elasticity along pathway (2).

As the easy core configuration is used as the reference for the energy variation, we define the total elastic correction $\Delta E^{\mathrm{el}}_{\mathrm{tot}}(\xi_2)$ as the difference between the elastic energy of the dislocation dipole at the reaction coordinate ξ_2, $E^{\mathrm{el}}_{\mathrm{tot}}(\xi_2)$, and the elastic energy of the easy core configuration $E^{\mathrm{el}}_{\mathrm{tot}}(easy)$. The total elastic energy stored in the simulation cell is calculated using anisotropic elasticity [55,56], taking into account the periodic boundary conditions [57]. The variation of the elastic energy along pathway (2), calculated in Fe, is shown in Fig. 13. The obtained variation is asymmetric, with the elastic correction being more important for the hard core than for the split core. To better understand this asymmetry, it is worth decomposing the variation of the elastic energy into two contributions.

The first contribution $\Delta E^{\mathrm{el}}_{\mathrm{PBC}}(\xi_2)$ corresponds to the elastic interaction between the two dislocations composing the dipole, as well as their interaction with all image dislocations introduced by periodic boundary conditions. This contribution is minimal when the dislocation periodic array corresponds exactly to a quadrupolar arrangement. This happens for $\xi_2 = 0.25$ as can be seen in Fig. 14. The position $\xi_2 = 0.5$ leads to the same dislocation periodic array as the one used for the easy core configuration. As a consequence, $\Delta E^{\mathrm{el}}_{\mathrm{PBC}}(\xi_2 = 0.5) = 0$. We also have $\Delta E^{\mathrm{el}}_{\mathrm{PBC}}(\xi_2 = 0) = 0$, in the hard core configuration, because of the combined

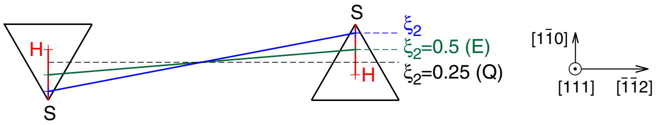

FIG. 14. (Color online) Schematic representation of three dislocation dipole configurations along pathway (2). The blue line represents a general configuration with a reaction coordinate ξ_2. The green line represents the dislocation dipole for $\xi_2 = 0.5$, which corresponds to the cut vector of the easy core configuration. The dashed black line represents the quadrupolar arrangement line, which corresponds to $\xi_2 = 0.25$.

TABLE V. Hard core energy calculated using DFT with two different periodicity vectors: hard $E_{H,\rm hard}$ and easy $E_{H,\rm easy}$. The energy calculated in the easy core reference frame is shown with and without elastic correction. They are given in meV/b.

	$E_{H,\rm hard}$	$E_{H,\rm easy}$	$E^{\rm corr}_{H,\rm easy}$
V	49.4	56.4	52.5
b	74.9	80.5	76.3
Ta	49.0	51.6	45.1
Mo	95.8	101.4	89.7
W	127.5	141.9	128.6
Fe	30.7	37.6	33.2

symmetry of the dislocation periodic array and of the bcc lattice leading to the same elastic energy for both the easy and the hard core configurations. Finally, the split core ($\xi_2 = 1$) leads to the highest contribution as this position is the furthest away from the plane corresponding to the quadrupolar arrangement (Fig. 14).

The second contribution $\Delta E^{\rm el}_{\varepsilon}(\xi_2)$ to the variation of the elastic energy arises from the use of fixed cell shape along the pathway. The total strain ε of the simulation cell is thus imposed, whereas the plastic strain contained in the cell varies when the distance between the two dislocations are moving. The elastic energy associated to this imposed strain ε is given by [29]:

$$E^{\rm el}_{\varepsilon} = h\left(\tfrac{1}{2}SC_{ijkl}\varepsilon_{ij}\varepsilon_{kl} + C_{ijkl}b_iA_j\varepsilon_{kl}\right), \tag{A1}$$

where S is the area of the simulation cell perpendicular to the dislocation lines, h the corresponding height, C_{ijkl} the elastic constants, and $\vec{A}$ the dipole cut vector. The latter is the only term that varies in Eq. (A1) when the dislocations move from one configuration to another on a given pathway, so that the variations of $\Delta E^{\rm el}_{\varepsilon}$ are linear along the hard to split pathway. As the hard core and the split core positions are equally separated from the easy core position, we can see in Fig. 13 that $|\Delta E^{\rm el}_{\varepsilon}(\xi_2 = 0)| = |\Delta E^{\rm el}_{\varepsilon}(\xi_2 = 1)|$.

Taking into account these two contributions, there is a partial compensation for the split core leading to a small total elastic correction $\Delta E^{\rm el}_{\rm tot}(\xi_2 = 1)$, whereas the elastic correction for the hard core is only due to the fixed cell shape and is thus more important.

2. Validation on DFT calculation of the hard core energy

The hard core energy was calculated with two different methods for all transition metals: the first method is the one used for the energy pathway (2), i.e. the hard core energy is calculated using the easy core periodicity vectors, corresponding to $q = 1/3m$ in Eq. (1) (denoted $E_{H,\rm easy}$) and corrected using anisotropy elasticity (denoted $E^{\rm corr}_{H,\rm easy}$). In the second method, the hard core energy is directly computed with the periodicity vectors adapted to this configuration, i.e. with $q = -1/3m$ in Eq. (1) (denoted $E_{H,\rm hard}$). The results are reported in Table V. One can see that $E_{H,\rm easy}$ is systematically larger than $E_{H,\rm hard}$ and is lowered by applying the elastic correction. The latter decreases the energy difference between $E_{H,\rm hard}$ and $E_{H,\rm easy}$ in all elements except in Ta and Mo where the energy difference remains constant, but goes from being positive ($E_{H,\rm hard} < E_{H,\rm easy}$) to negative ($E_{H,\rm hard} > E^{\rm corr}_{H,\rm easy}$).

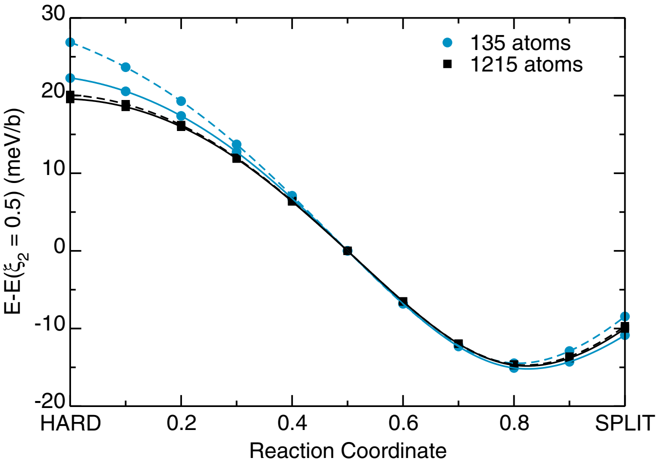

FIG. 15. (Color online) Energy profile along pathway (2) calculated in Fe with Marinica EAM potential [23] for two cell sizes, 135 and 1215 atoms. The dashed lines are the energy profiles before elastic correction and the full lines are the corrected profiles.

3. Validation on EAM calculation for two cell sizes

A validation for the calculation of the elastic correction was also performed on the energy profile along pathway (2) in Fe, using the EAM potential developed by Marinica *et al.* [23]. The calculations were performed using the same dislocation dipole configuration as presented in Sec. IIA, but using two different cell sizes, 135 and 1215 atoms/b. One can see in Fig. 15 that the elastic correction decreases when the size of the cell increases. The correction is nonnegligible for the 135 atom cell and brings the energy profile close to that obtained in the 1215 atom cell, where the correction is negligible.

[1] V. Vitek, Cryst. Latt. Def. **5**, 1 (1974).
[2] J. W. Christian, Metall. Trans. A **14**, 1237 (1983).
[3] D. Caillard and J. L. Martin, *Thermally Activated Mechanisms in Crystal Plasticity* (Pergamon Press, Oxford, 2003).
[4] P. Guyot and J. E. Dom, Canad. J. Phys. **45**, 983 (1967).
[5] H. Koizumi, H. O. K. Kirchner, and T. Suzuki, Acta Mater. **41**, 3483 (1993).
[6] D. Rodney and L. Proville, Phys. Rev. B **79**, 094108 (2009).
[7] P. A. Gordon, T. Neeraj, Y. Li, and J. Li, Modelling Simul. Mater. Sci. Eng. A **18**, 085008 (2010).
[8] D. Gröger and V. Vitek, Modelling Simul. Mater. Sci. Eng. **20**, 035019 (2012).
[9] L. Proville, L. Ventelon, and D. Rodney, Phys. Rev. B **87**, 144106 (2013).

[10] M. Mrovec, D. Nguyen-Manh, C. Elsässer, and P. Gumbsch, Phys. Rev. Lett. **106**, 246402 (2011).

[11] L. Ventelon and F. Willaime, J. Computed-Aided Mater. Des. **14**, 85 (2007).

[12] M. Itakura, H. Kaburaki, and M. Yamaguchi, Acta Mater. **60**, 3698 (2012).

[13] L. Ventelon, F. Willaime, E. Clouet, and D. Rodney, Acta Mater. **61**, 3973 (2013).

[14] C. R. Weinberger, G. J. Tucker, and S. M. Foiles, Phys. Rev. B **87**, 054114 (2013).

[15] M. Duesbery and V. Vitek, Acta Mater. **46**, 1481 (1998).

[16] K. Edagawa, T. Suzuki, and S. Takeuchi, Phys. Rev. B **55**, 6180 (1997).

[17] K. Edagawa, T. Suzuki, and S. Takeuchi, Mat. Sci. Eng. A **234**, 1103 (1997).

[18] R. Gröger and V. Vitek, Acta Mater. **56**, 5426 (2008).

[19] S. Takeuchi, Philos. Mag. A **39**, 661 (1979).

[20] M. I. Mendelev, S. Han, D. J. Slorovitz, G. J. Ackland, D. Y. Sun, and M. Asta, Philos. Mag. **83**, 3977 (2003).

[21] G. J. Ackland, L. I. Mendelev, D. J. Srolovitz, S. Han, and A. V. Barashev, J Phys.: Condens. Matter **16**, S2629 (2004).

[22] H. Chamati, N. I. Papanicolaou, Y. Mishin, and D. A. Papaconstantopoulos, Surf. Sci. **600**, 1793 (2006).

[23] L. Proville, D. Rodney, and M.-C. Marinica, Nat. Mater. **11**, 845 (2012).

[24] M.-C. Marinica, L. Ventelon, M. R. Gilbert, L. Proville, S. L. Dudarev, J. Marian, G. Bencteux, and F. Willaime, J. Phys.: Condens. Matter **25**, 395502 (2013).

[25] P. Giannozzi, S. Baroni, N. Bonini, M. Calandra, R. Car, C. Cavazzoni, D. Ceresoli, G. Chiarotti, M. Cococcioni, I. Dabo, A. Dal Corso, S. de Gironcoli, S. Fabris, G. Fratesi, R. Gebauer, U. Gerstmann, C. Gougoussis, A. Kokalj, M. Lazzeri, L. Martin-Samos, N. Marzari, F. Mauri, R. Mazzarello, S. Paolini, A. Pasquarello, L. Paulatto, C. Sbraccia, S. Scandolo, G. Sclauzero, A. P. Seitsonen, A. Smogunov, P. Umari, and R. M. Wentzcovitch, J. Phys.: Condens. Matter **90**, 395502 (2009).

[26] L. Ventelon, F. Willaime, C.-C. Fu, M. Heran, and I. Ginox, J. Nucl. Mater. **425**, 16 (2012).

[27] R. Soulairol, C.-C. Fu, and C. Barreteau, J. Phys.: Condens. Matter **22**, 295502 (2010).

[28] J. Li, C. Z. Wang, J. P. Chang, W. Cai, V. V. Bulatov, K. M. Ho, and S. Yip, Phys. Rev. B **70**, 104113 (2004).

[29] E. Clouet, L. Ventelon, and F. Willaime, Phys. Rev. Lett. **102**, 055502 (2009).

[30] S. Ismail-Beigi and T. A. Arias, Phys. Rev. Lett. **84**, 1499 (2000).

[31] C. Woodward and S. I. Rao, Phys. Rev. Lett. **88**, 216402 (2002).

[32] S. L. Frederiksen and K. W. Jacobsen, Philos. Mag. **83**, 365 (2003).

[33] C. Domain and G. Monnet, Phys. Rev. Lett. **95**, 215506 (2005).

[34] G. Henkelman, G. Johannesson, H. Jonsson, *Progress on theoretical chemistry and physics* (Kluwer Academic Publishers, Dordrecht, 2000).

[35] E. Clouet, Phys. Rev. B **84**, 224111 (2011).

[36] L. Louail, D. Maouche, A. Roumili, and F. Ali Sahraoui, Mater. Lett. **58**, 2975 (2004).

[37] L. Koci, Y. Ma, A. R. Oganov, P. Souvatzis, and R. Ahuja, Phys. Rev. B **77**, 214101 (2008).

[38] D. I. Bolef, J. Appl. Phys. **32**, 100 (1961).

[39] D. I. Bolef and J. De Klerk, J. Appl. Phys. **33**, 2311 (1962).

[40] D. J. Dever, J. Appl. Phys. **43**, 3293 (1972).

[41] K. J. Caroll, J. Appl. Phys. **36**, 3689 (1965).

[42] D. I. Bolef and J. De Klerk, Phys. Rev. **129**, 1063 (1963).

[43] C. Kittel, *Introduction to Solid State Physics* (Wiley, New York, 1967).

[44] E. Clouet, L. Ventelon, and F. Willaime, Phys. Rev. B **84**, 224107 (2011).

[45] F. Willaime, A. Satta, M. Nastar, and O. Le Bacq, Int. J. Quantum Chem. **77**, 927 (2000).

[46] A. Satta, F. Willaime, and S. de Gironcoli, Phys. Rev. B **57**, 11184 (1998).

[47] A. Satta, F. Willaime, and S. de Gironcoli, Phys. Rev. B **60**, 7001 (1999).

[48] J. Chaussidon, M. Fivel, and D. Rodney, Acta Mater. **54**, 3407 (2006).

[49] T. Suzuki, Y. Kamimura, and H. O. K. Kirchner, Philos. Mag. A **79**, 1629 (1999).

[50] S. Takeuchi, T. Hashimoto, and K. Maeda, Trans. Jpn. Inst. Met. **23**, 60 (1982).

[51] S. Takeuchi and K. Maeda, Acta. Metall. **25**, 1485 (1977).

[52] L. Hollang, D. Brunner, and A. Seeger, Mater. Sci. Eng. A **319-321**, 233 (2001).

[53] D. Brunner, Mater. Trans. JIM **41**, 152 (2000).

[54] D. Brunner and J. Diehl, Phys. Stat. Sol. A **160**, 355 (1997).

[55] A. N. Stroh, Philos. Mag. **3**, 625 (1958).

[56] A. N. Stroh, J. Math. Phys. (Cambridge, Mass.) **41**, 77 (1962).

[57] W. Cai, V. V. Bulatov, J. Chang, J. Li, and S. Yip, Philos. Mag. **83**, 539 (2003).